Influence of rare earth oxides on kinetics and reaction mechanisms in CMAS silicate melts

François Perrudin, Marie-Hélène Vidal-Sétif, Catherine Rio, Carine Petitjean, Pierre-Jean Panteix, Michel Vilasi

Influence of rare earth oxides on kinetics and reaction mechanisms in CMAS silicate melts

F. Perrudin[a,b*], M. H. Vidal-Sétif [a], C. Rio[a], C. Petitjean[b], P.J. Panteix[b], M. Vilasi[b]

[a] *ONERA / DMAS, Université Paris Saclay, F-92322 Châtillon, France*
[b] *Université de Lorraine, CNRS, IJL, F-54000 Nancy, Fance*

Abstract

Dissolution of different rare earth oxides RE_2O_3 and cyclosilicate $Ca_3RE_2(Si_3O_9)_2$ was studied at 1200°C in a pseudo-ternary CAS melt. This investigation is relevant to CMAS resistant thermal barrier coatings (TBC) used in aircraft engines. CMAS is a generic term for the molten siliceous deposits resulting from the ingestion of mineral particles with the intake air. The aim was to assess the influence of the rare earth on the reaction kinetics, solubility limits and underlying phase equilibria in a model CAS melt. RE_2O_3 (RE = Nd, Sm, Gd, Dy and Yb) were selected to span a wide range of trivalent lanthanide sesquioxides and Lewis basicities. Powders dispersed in CAS glass-beads were reacted at 1200°C and quenched after several durations. All the RE_2O_3 led to the formation of metastable apatite, and then to stabilization of cyclosilicate in CAS. Disilicate $Yb_2Si_2O_7$ was also obtained in Yb_2O_3 bead-sample during early-stage of interaction. However, RE_2O_3 oxide basicity has a direct influence on silicates (apatite, disilicate and cyclosilicate) solubility limits in CAS, on RE-apatite crystal growth as well as on induction time for RE-cyclosilicate nucleation. The results are discussed in the light of crystal chemistry, thermodynamic considerations and RE cation field strength (Z/r^2) which is alternative to define oxide basicity.

Keywords: Thermal Barrier Coatings (TBC), CMAS, Rare earth, Solubility, Kinetics

[*]Corresponding author at: 29 avenue de la Division Leclerc, 92322, Châtillon, France.
Tel.: +33 1 46 73 44 70 ; fax: +33 1 46 73 41 64
E-mail addresses: francois.perrudin@onera.fr (F. Perrudin) ; marie-helene.vidal-setif@onera.fr (M. H. Vidal-Sétif) ; catherine.rio@onera.fr (C. Rio) ; carine.petitjean@univ-lorraine.fr (C. Petitjean) ; pierre-jean.panteix@univ-lorraine.fr (P. J. Panteix) ; michel.vilasi@univ-lorraine.fr (M. Vilasi).

1. Introduction

Fine contaminants as sand, dust or volcanic ashes ingested by aircraft engines are well-known to induce damage in standard Thermal Barrier Coatings (TBC, ZrO_2-8wt. %Y_2O_3). In service, these mineral particles deposit on hot TBC surface (≥ 1200°C) as molten silicate and infiltrate porous microstructure of coating [1-4]. Composition of silicate deposits closely depends on their geological source and their transport across continents when suspended in the atmosphere. Analysis of ex-service components reveal that, in addition to primary silica (SiO_2), alumina (Al_2O_3), alkaline-earth oxides (CaO, MgO), but also metallic oxides (TiO_2, FeO_x) are generally found in varying proportions [5-7].

Model silicate deposits limited to a few constituents (CMAS, i.e. CaO-MgO-Al_2O_3-SiO_2) are thus mainly employed in the laboratory to study the thermochemical interaction with novel TBC compositions which potentially inhibit CMAS infiltration. Many tests are conducted under isothermal conditions for simplicity thus neglecting thermal gradient across TBC. In addition to deposition technology (Electron-Beam Physical Vapor Deposition (EB-PVD), Atmospheric (APS) and Suspension Plasma Spray (SPS)), dense ceramic pellets or less frequently powders are also used to simulate TBC coating material. Gadolinium zirconate $Gd_2Zr_2O_7$ TBC has first shown efficiency to mitigate synthetic CMAS infiltration due to its reactivity with CMAS. Indeed, the dissolution reaction leads to the extremely fast and simultaneous formation, in the TBC flow channels (intercolumnar gaps for EB-PVD coatings), of a sealing-layer constituted of crystalline zirconia $Zr(Ca,Gd)O_x$ and $Ca_2Gd_8(SiO_4)_6O_2$ apatite [8]. Most of rare earth oxides RE_2O_3 can replace yttria in ZrO_2-based TBC as both zirconia and apatite phases can accommodate a broad range of lanthanide elements within their structures [9-10].

However, little is known about phase equilibria involving TBC constituents (ZrO_2, RE_2O_3) and multi-component CMAS system. In this context, Poerschke *et al.* have previously proposed a thermodynamic study of the CaO-SiO_2-RE_2O_3 subsystem (RE = Y and Gd) at 1400°C [11,12]. It appeared that Gd-cyclosilicate phase $Ca_3Gd_2Si_6O_{18}$ is in equilibrium with liquid phase to the detriment of Gd-apatite phase. The present work is intended to determine which precipitated phases are in equilibrium with the liquid at 1200°C (typical temperature of TBC surface) in the case of rare earths in contact with a simplified CaO-Al_2O_3-SiO_2 melt. As the identified phases do not contain alumina, although Al (like other species of CMAS and

TBC) may redirect the dissolution pathway, this study relies on the diagrams produced by Poerschke *et al.* [11,12], which indicate that low concentrations of rare earth oxide are required to remain in equilibrium with the liquid.

In a previous authors' work [13], the relative stability of the precipitated Gd-apatite and Gd-cyclosilicate phases was investigated. Their own dissolution reactions in eutectic CaO-Al_2O_3-SiO_2 (CAS) melt at 1200°C, as well as that of Gd_2O_3, systematically led to Gd-cyclosilicate phase in equilibrium with CAS melt for long interaction times. Conversely, Gd-apatite crystals formed at Gd_2O_3/CAS interface during early-stage were in metastable equilibrium with CAS melt. It has also been shown that other rare earth silicates may compete with apatite crystallization and a change in RE solubility limit may result depending on both RE_2O_3 and CMAS composition. Garnet silicate, orthosilicate $Ca_3RE_2Si_3O_{12}$ as well as disilicate $RE_2Si_2O_7$ phases have been previously reported as CMAS/TBC reaction product [14-17]. Re-precipitation of zirconia ZrO_2 containing RE and/or Ca in solid solution has been regularly observed when the Zr saturation limit in the melt is exceeded [15-19] whereas zircon $ZrSiO_4$ or Ca,Zr-rich phases were occasionally noticed [15,16,18,19]. These two kinds of crystallization reactions also induce modification of the melt composition leading to intrinsic precipitation of Zr,RE-free silicates. Anorthite $CaAl_2Si_2O_8$, diopside $CaMgSi_2O_6$ and melilite $Ca_2(Mg,Al)[(Al,Si)SiO_7]$ are current examples of the many phases which can be precipitated [13-15]. In our previous work [13], chemical analysis of CAS melt (1200°C) composition over time also evidenced the local enrichment in Al induced by Gd-apatite formation which further led to anorthite precipitation.

Nevertheless, phase equilibria only provide information on overall crystallization reaction and are thus relevant to coating chemical durability in CMAS melts once their infiltration is stopped. Thermodynamic data, therefore, do not determine the efficiency of CMAS infiltration mitigation which occurs during early-stage of interaction. Indeed, local and non-equilibrium conditions during short times involve the appearance of metastable phase(s) before the formation of stable phase(s). Kinetics considerations are also a fundamental requirement to understand CMAS/TBC interaction.

This study deals with the dissolution of different rare earth single (RE_2O_3) and multi-metal oxide (RE-apatite or RE-cyclosilicate) in eutectic CAS melt (1200°C) using powders dispersed in glass-beads. These investigations are a continuation of previous work dealing

with the Gd_2O_3 dissolution mechanisms in CAS. The aim is to assess the influence of rare earth (relative to Gd_2O_3) on reaction kinetics, solubility limit and underlying phase equilibria in the CAS melt. For this, Nd_2O_3, Sm_2O_3, Dy_2O_3 and Yb_2O_3 were first selected to cover a wide range of Lewis oxide basicity. Then, multiple annealing times and quenching were performed to provide information on kinetics in a timescale compatible with early stage of CMAS/TBC interaction as well as on phase equilibria for longer times. Powder XRD and SEM-EDS analysis were employed for phase identification while amounts of RE dissolved in CAS were measured overtime by EPMA. The results are discussed in the light of crystal chemistry, thermodynamic considerations and RE cation field strength (Z/r^2) which is alternative to define oxide basicity.

2. Experimental procedures

2.1 Precursor materials

The pseudo-ternary eutectic (1170°C) composition, $58.9SiO_2$-$16.9AlO_{1.5}$-$24.1CaO$ mol. % ($61.5SiO_2$-$15Al_2O_3$-$23.5CaO$ wt. %, CAS), was selected in this study as CMAS melt subsystem. The choice of this simplified CAS composition as well as the details on glass preparation are reported in a previous work [19]. Glass was obtained from suitable proportions of $CaCO_3$ (99%, Prolabo), Al_2O_3 (99.7%, Cerac) and amorphous SiO_2 (99.9%, Aldrich) raw reagents.

Commercial powders of rare-earth oxides RE_2O_3 were used as starting solute for the dissolution experiments in CAS melt. Their characteristics given by the suppliers are summarized in table 1. These compositions were selected to span a wide range of trivalent lanthanide sesquioxides and Lewis basicities.

Rare-earth cyclosilicate powders with $Ca_3RE_2(Si_3O_9)_2$ composition were prepared by solid state reaction between rare-earth oxides, calcium carbonate $CaCO_3$ and SiO_2 reagent powders. Two steps of 6h-calcination at 1400°C were performed with intermediate regrinding to achieve homogeneous mixture and promote surface contact area between particles. Finally, nitric acid HNO_3 was added to the resulting RE-cyclosilicate powders and a vacuum filtration wash was performed to remove unreacted RE_2O_3 powders [20].

2.2 Dissolution experiment and equilibration

The procedure used to study the dissolution of rare earth oxides or cyclosilicates in CAS has been described in a previous work [13]. First, CAS-glass beads containing dispersed RE_2O_3 or RE-cyclosilicate powder were elaborated at 1200°C. Then bead samples were suspended with a Pt wire and annealed in air at 1200°C, for durations from 5 min to ≥ 72 h. They were finally quenched in air to retain the high-temperature configuration. Short duration intervals (from 5 min to 1h30 annealing) were performed to provide information on kinetics in a timescale compatible with the early stage of CMAS/TBC interaction. Conversely, long-term annealing (up to 160h) was performed to attempt achieving equilibrium between the liquid and the precipitated phases dictated by thermodynamics.

The ternary phase diagrams of the $CaO\text{-}SiO_2\text{-}REO_{1.5}$ (with RE = Gd or Y) system show that the addition of low quantities of rare earth oxide is required to obtain a solid-liquid equilibrium [11,12]. Consequently, 2 to 6 mol. % of $REO_{1.5}$ have been added to CAS beads, which corresponds to a range 10 to 15 wt. % for the different rare earths studied here and up to 60 wt. % for the RE-cyclosilicates. The latter case leads to lower Al content and equivalent RE content compared to the addition of RE_2O_3. The amount of introduced powder was adjusted in order to observe a solid-liquid equilibrium. The overall compositions of these mixtures are reported in the table 2, for Nd and Yb only, as they cover the larger range of composition for a given amount of RE_2O_3 or RE-Cyclosilicate.

2.3 Sample preparation and characterization

Cross-sections of the beads mixture containing RE-oxide were prepared after epoxy embedding, successive polishing to ¼ µm and carbon coating. Backscattered electron imaging (BSE, Zeiss DSM962 SEM) was used to characterize the microstructure of each RE-oxide/CAS bead after annealing, and more precisely to have a first estimation of the amount, the morphology and the size of the precipitated phases. Elemental composition of the various phases was measured using energy dispersive spectroscopy in the SEM (SEM-EDS, Kevex Quantum type EDS analyzer).

Electron Probe Micro-Analyzer (EPMA) CAMECA SX100 was employed to quantify the amount of rare earth cation RE^{3+} which was dissolved in CAS beads. For this, RE elements as

well as Ca, Al and Si were analyzed at 10 µm of the precipitated RE-silicates. This vicinity involves a short period of chemical diffusion and ensures the measurement of the highest RE content in the glass matrix for short times. The results of the quantification are averaged from 10 measurements and the error bars correspond to standard deviations.

When large enough, the RE-rich precipitates were also probed to establish their composition. The conditions used for microanalysis were an accelerating voltage of 15 kV, a focused beam current of 10 nA and a time analysis of 15 s per element. The used standards were andradite $Ca_3Fe_2(SiO_4)_3$ for Ca, alumina for Al, albite $NaAlSi_3O_8$ for Si, lanthanide sesquisulfide RE_2S_3 for Yb, Dy, Gd and lanthanide phosphate $REPO_4$ for Sm, Nd.

X-Ray Diffraction (XRD) data were collected on a Empyrean diffractometer using Cu Kα emission ($\lambda_{K\alpha}$=0.15406 nm) in a 2θ range from 10 to 90°(2θ). In order to get a higher resolution of the X-ray diffractograms, the CAS samples were prepared here with addition of amounts of rare earth oxide increased to 30 wt. %, which corresponds to 11 to 13 mol. % of $REO_{1.5}$ (depending on the considered rare earth). Indeed, the pseudo-ternary phase diagrams of the CaO-SiO_2-$REO_{1.5}$ (with RE = Gd or Y) system [11,12] shows that a light increase of the mol. % of $REO_{1.5}$ does not modify the nature of the phases but only their relative proportions. Anyway, the nature of the different phases was verified via SEM observation before XRD analysis. Diffraction patterns were recorded with a step interval of 0.0167°(2θ). For this analysis, all the samples were grounded in fine powder to reduce preferential orientation. Indexation of XRD patterns using ICDD crystallographic database (PANanlytical XPERT HighScore) was first performed for crystalline phases identification. Rietveld refinement from the RE-oxide/CAS diffraction data was then performed by the mean of Fullprof Suite software. The relative volume fraction of RE-silicate phases was subsequently quantified regardless of amorphous content.

3. Results

3.1 Phase evolution during CAS / RE_2O_3 interaction

3.1.1 Short-times interaction

Back-Scattered SEM images resulting from interaction of different RE_2O_3 powders with CAS melt are shown in Fig. 1 and Fig. 2 after 5 min dwell-time at 1200°C. Based on overall observation, it can be first noticed that RE_2O_3 agglomerates (bright contrast) never

coexist directly with the CAS melt. Indeed, a solid interphase composed of RE-apatite separates all RE_2O_3 powders from the melt. This phase was identified by the combination of XRD and EDS analysis. Hexagonal structure with $P6_3/m$ space group was obtained for all RE-apatite. Indeed, the alkaline-earth (Ca^{2+}) apatite structure is well-known to accommodate complete lanthanide series [9]. Both cations Ca^{2+} and RE^{3+} are distributed within the 4f (CN 9) and 6h (CN 7) sites. A wide range of Ca^{2+}/RE^{3+} substitution in RE-apatite may also be obtained considering the existence of cation vacancies and/or oxygen vacancies [9].

Variation in the size and the morphology of RE-apatite precipitates can also be observed between the different RE_2O_3. The SEM micrographs display a change in the shape of RE-apatite from a thin-nearly continuous layer for Yb_2O_3 (Fig. 2b) to a conglomerate of needle-like crystals for Nd_2O_3 (Fig. 1a). This latter acicular arrangement for apatite was commonly found in various glass-ceramic and is often associated with a preferential growth aligned along the c axis [21]. An intermediate RE-apatite microstructure was obtained for Dy_2O_3 (Fig. 1d), Gd_2O_3 (Fig. 1c) and Sm_2O_3 (Fig. 1b). It consists in elongated crystals growing outwardly from a thin denser layer at the RE_2O_3 interface. After 5 min, several stages of apatite crystal growth (in terms of acicularity) can be observed between the different RE_2O_3 and appear to be enhanced in the following order $Yb_2O_3 < Dy_2O_3 < Gd_2O_3 < Sm_2O_3 < Nd_2O_3$. Moreover, it can be noticed that the amount of RE_2O_3 that already reacted globally increases on the whole sample according to $Yb_2O_3 < Dy_2O_3 < Gd_2O_3 < Sm_2O_3 < Nd_2O_3$. For the CAS-bead mixture containing Nd_2O_3, almost all the initial powder was already converted into Nd-apatite. This is another evidence of the relative trend in forming RE-apatite in CAS melt. It can be concluded from these short time interactions that the formation of apatite is favored for rare earths with larger ionic radius.

In addition to RE-apatite, a second RE-rich silicate phase was detected in both Dy_2O_3 and Yb_2O_3 samples. This phase was identified as RE-cyclosilicate $Ca_3RE_2(Si_3O_9)_2$ crystallizing in the monoclinic structure with C2/c space group. Only a limited amount of Dy-cyclosilicate was noticed in CAS compared to Yb-cyclosilicate crystals which were abundantly found. Previous work already showed that Gd_2O_3 indirectly dissolved in CAS by first forming very rapidly Gd-apatite, which gradually redissolved in CAS before precipitating stable $Ca_3Gd_2(Si_3O_9)_2$ cyclosilicate [13]. The same kind of mechanism is here observed for the Dy_2O_3 and Yb_2O_3 samples. The location, for short times, of Yb and Dy-cyclosilicate around RE-apatite crystals is suggestive of very fast cyclosilicate germination kinetics (less

than 5 min for Yb and Dy-cyclosilicate). For Yb_2O_3 samples, another Yb-silicate with same BSE chemical contrast as Yb-apatite was observed as well as a Yb-free aluminosilicate (crystals in darker contrast than CAS matrix) (Fig. 2a-b). These both phases located in the apatite-rich regions were respectively identified as $Yb_2Si_2O_7$ disilicate and $CaAl_2Si_2O_8$ anorthite using EDS elemental maps (Fig. 2c-d) and XRD analysis. Some Yb_2O_3 was also found as inclusions inside disilicate phases suggesting a competitive crystallization between Yb-disilicate and Yb-apatite at the Yb_2O_3/CAS interface. The crystalline structure of the disilicate phase was indexed with the monoclinic C2/m space group and the anorthite crystallizes with a triclinic (P-1) structure. After 5 min, Yb_2O_3, Yb-apatite, $Yb_2Si_2O_7$ and $CaAl_2Si_2O_8$ solid phases are thus coexisting with residual CAS melt in a limited area entirely surrounded by Yb-cyclosilicate. Anorthite intrinsic precipitation from CAS melt has already been observed after a local enrichment in Al_2O_3 induced by CaO and SiO_2 depletion during RE-silicate formation [13, 18]. Disilicate ($Y_2Si_2O_7$) formation was already reported elsewhere, resulting from 1300°C isothermal interaction between yttria and CAS melt ($70SiO_2$-$15AlO_{1.5}$-15CaO mol.%) with lower content of CaO [15]. Thermodynamics Y_2O_3-Al_2O_3-SiO_2 phase diagram also reveals that $Y_2Si_2O_7$ is in equilibrium with the liquid phase in the Al_2O_3-lean region [22]. Therefore, a decrease in CaO and Al_2O_3 activity in CAS melt arising from concomitant crystallization of Ca and Al-rich phases may explain Yb-disilicate formation.

3.1.2 long-times interaction

Results from the dissolution sequence of the different RE_2O_3 after 72h annealing time at 1200°C are shown in Fig. 3. Yb_2O_3 is not presented here as no changes in the phase identity and the local arrangement could be noticed after 5 min. Indeed, the Yb-cyclosilicate phase is surrounding the various Yb-silicates and thus limits their contacts with the melt, consequently leading to a much slower evolution.

It can be first observed that anorthite crystals (dark contrast) in the CAS matrix were present in all samples. As discussed for short times, its formation is the consequence of an Al-enrichment of CAS melt due to the precipitation of RE silicates.

For Gd_2O_3 and Dy_2O_3, RE-apatite phase (Fig. 3a-b) was fully converted into RE-cyclosilicate during 72h interaction time. Dy-cyclosilicate crystal growth was observed between 5 min and 72h (Fig. 1-d compared to Fig. 3-b) with a crystal size increasing from few

microns to several tens microns. In our previous work, a similar change in Gd-cyclosilicate crystal size was noticed between 1h30 and 72h dwell-time at 1200°C [13].

Conversely, RE-apatite in Sm_2O_3 and Nd_2O_3 samples (Fig. 3c-d) was still remaining in CAS melt with a characteristic needle shape in both cases. Cyclosilicate crystals rich in Sm and Nd were still not detected in CAS melt after 72h. With increasing time, some Sm-cyclosilicate crystals finally appeared after 160h of isothermal treatment (1200°C) and were located relatively far away from the apatite-rich region (Fig. 3f). The size of these cyclosilicate crystals was larger than Yb, Gd and Dy-isomorphs and nearly reached the hundred microns. No Nd-cyclosilicate crystals could be detected in the Nd_2O_3/CAS bead after 160h which may suggest a delayed nucleation over time.

The duration of the different steps in the reaction sequence during RE_2O_3 dissolution (1200°C) are summarized in table 3. It can be seen first that the annealing times required to completely dissolve initial RE_2O_3 powders globally decreases from Yb_2O_3 to Nd_2O_3. For Yb_2O_3, competitive formation of Yb-apatite and $Yb_2Si_2O_7$ disilicate occurred during the early-stage of interaction between the oxide powder and the CAS melt. Moreover, Yb-cyclosilicate crystals were also observed in a great extent in less than 5 min. Thus, many initial oxide powders remain trapped in those solid phases, resulting in longer time to be dissolved. Conversely, Nd_2O_3 powders were fully converted into Nd-apatite in short time interaction and no Nd-cyclosilicate crystals could be detected after 160h. The reactivity of Dy_2O_3, Gd_2O_3 and Sm_2O_3 with CAS to crystallize RE-apatite and then precipitate cyclosilicate from the melt was intermediate. It appears here that for long time CAS/RE_2O_3 interactions the formation of cyclosilicate is favored for rare earths with smaller ionic radius.

3.1.3 Cyclosilicate crystallization kinetics

To confirm the trends observed above on RE-cyclosilicate crystallization kinetics in CAS melt, the relative proportions (in volume fraction and weight fraction) of crystalline RE-silicates (1200°C) were also quantified after 1h-annealing by XRD Rietveld refinement regardless of the amorphous phase. In figure 4a, an example of XRD pattern after refinement is given for Gd_2O_3 sample. It can be seen from the residual curve that the calculated pattern accurately fits experimental data in the 10-80° (2θ) range. The other refinements performed on the different RE_2O_3/CAS diffractograms were also suitable for phase indexation and phase quantification. Recalculated Bragg peaks position for RE-cyclosilicate compounds was

consistent with the available $Ca_3Y_2(Si_3O_9)_2$ crystalline structure data [23]. The volume fraction of the different RE-silicates dispersed in the whole sample is reported in a diagram (Fig. 4b). In addition, it can be noticed that the increase in the amount of RE_2O_3 to 30 wt.% does not modify the nature of the precipitated phases compared to the previous CAS-bead samples.

For Nd_2O_3 and Sm_2O_3, quantification results in 100 vol. % of crystalline RE-apatite which is consistent with the observed absence of RE-cyclosilicate precipitation in glass beads in this time scale. The RE-apatite proportion in Gd_2O_3 and Dy_2O_3 samples decreases respectively to 83 and 51 vol. % fraction (i.e. 89 and 63 wt. %). Conversely, the volume fraction of RE-cyclosilicate which crystallizes increases to respectively 17 and 49 vol. % (i.e. 11 and 37 wt. %) for Gd_2O_3 and Dy_2O_3. Phase quantification for Yb_2O_3 yields the highest amount of precipitated Yb-cyclosilicate (52 vol. % i.e. 40 wt. %) and the presence of $Yb_2Si_2O_7$, Yb-apatite at 20 vol. % and 29 vol. % (i.e. 23 wt. % and 37 wt. %) respectively. This clearly confirms the favorable tendency toward forming RE-cyclosilicate in the order Nd_2O_3<Sm_2O_3<Gd_2O_3<Dy_2O_3< Yb_2O_3.

3.2 Dissolution kinetics and solubility limits

3.2.1 Indirect RE_2O_3 dissolution

The RE content (in at. %) dissolved in CAS melt in RE_2O_3/CAS samples was measured by EPMA for durations comprised between 5 min and 72h. The evolution of this content as a function of the square root of time was then plotted in figure 5. Due to differences in crystallization kinetics previously described, spot analyses were performed in the vicinity of different RE-silicates (at 10 µm) according to the considered RE_2O_3.

The high dispersion in the values of RE amount for all RE_2O_3 during early stage of dissolution can be noticed from standard deviation (resulting from 10 analyses) in figure 5 a-b. This indicates that RE is still not homogeneously incorporated on the whole sample within the 10 µm area. For longer times, local equilibrium conditions between CAS melt and RE-silicates are attained resulting in very low dispersion values.

The evolution of Gd amount in CAS melt with time (Fig. 5a) has already been described and analysed in a previous work [13]. The rapid rise in Gd content during short times durations is associated with Gd-apatite dissolution as it quickly surrounds the initial

Gd_2O_3. This metastable phase sufficiently remains in contact with CAS melt over time to reach a saturation concentration i.e. Gd-apatite solubility limit. For longer times (> 4h) Gd-cyclosilicate precipitation and growth lead to a drop in Gd amount in CAS melt tending toward new equilibrium concentration. Measurements for Nd_2O_3 and Sm_2O_3 (Fig. 5a), only provide information on RE-apatite crystals dissolution. For both oxides, a concentration plateau is quickly reached before 4h indicating that dissolution kinetics is relatively high. This saturation value is related to metastable equilibrium between RE-apatite and CAS melt. A drop in RE amount induced by RE-cyclosilicate precipitation would be expected for longer times, as for Gd_2O_3. For Dy_2O_3 and Yb_2O_3 (Fig. 5b), a rapid crystallization of RE-cyclosilicate occurs for very short times in addition to the precipitation of apatite. The kinetics thus corresponds to a slower equilibration process. Saturation plateau is reached after 4h and 8h for Dy_2O_3 and Yb_2O_3 respectively. The RE saturation concentration in the melt for the different RE_2O_3 as well as CAS composition are reported in table 4.

These saturation values may be associated to RE-apatite solubility limit in CAS for Gd_2O_3, Sm_2O_3 and Nd_2O_3. For Yb_2O_3 and Dy_2O_3 the saturation values cannot be reliably assigned to the RE-cyclosilicate solubility limit. Indeed, successive and independent measurements around RE-apatite and RE-cyclosilicate were not achievable as both RE-silicate phases were present for short times. The RE amount incorporated in CAS melt at 1200°C increases in the order $Yb_2O_3 < Dy_2O_3 < Gd_2O_3 < Sm_2O_3 < Nd_2O_3$. In addition, it must be noted that the composition of the CAS melt is lightly modified due to the dissolution of rare earth oxides and to the precipitation of silicate phases. However, no significant variation in CAS melt composition is observed between the different RE_2O_3 despite the precipitation of different silicate phases (RE-apatite or RE-cyclosilicate). This is in agreement with the 1200°C isothermal section of CAS diagram predicting a narrow liquid region around eutectic composition [24]. For all RE_2O_3, anorthite is precipitated and observed to be in equilibrium with CAS melt containing up to 6.50 at. % of Al.

3.2.2 Direct dissolution of synthetic RE-cyclosilicate

Experiments in section 3.1 showed that interactions between RE_2O_3 and CAS led to the stabilization of RE-cyclosilicate whatever the considered RE was (assuming Nd_2O_3 would also form Nd-cyclosilicate in CAS). However, RE-cyclosilicate solubility limit could not be properly determined in the timescale. Indeed, RE-cyclosilicate precipitation is never observed

for Nd, and after a very long duration (160h) for Sm. For Yb and Dy samples, the RE content in melt is the result of the different RE-silicates dissolution, which might also involve important changes in the CAS composition. Thus, the melt composition may correspond to RE oversaturation due to apatite or disilicate dissolution and uncertainties remain if the RE equilibrium saturation for cyclosilicate is reached in such device after long-term exposure at 1200°C.

It is therefore required to also study RE-cyclosilicate crystals dissolution in CAS melt. For this, CAS-bead mixtures containing the different RE-cyclosilicate powders (previously elaborated via solid state synthesis) were annealed at 1200°C for various durations.

SEM observations (not shown here) reveal that direct dissolution took place between the synthesized RE-cyclosilicate and CAS melt. Moreover, the dissolution of the different RE-cyclosilicates did not lead to intrinsic crystallization of CAS melt. For longer times up to 144h, RE-cyclosilicate was the unique phase finally coexisting with CAS melt in all samples. This may confirm previous observations made on RE_2O_3/CAS beads which suggested a thermodynamic equilibrium between RE-cyclosilicate and CAS melt at 1200°C. However, the final CAS melt composition has to be comparable in both cases to validate such a statement.

Therefore, EPMA measurements were also performed in the vicinity of RE-cyclosilicate during dissolution process. The evolution of RE content dissolved in CAS melt *vs.* square root of time is reported on Fig. 6 a-b for various RE-cyclosilicate/CAS mixtures. For all samples, time to reach RE equilibrium concentration varies according to the considered RE-cyclosilicate. Indeed, equilibration kinetics of Yb and Dy-cyclosilicate in CAS (Fig. 6b) are faster than for Nd, Sm-cyclosilicate and in a lesser extent than for Gd-cyclosilicate (Fig. 6a). An increasing saturation value referring to RE-cyclosilicate solubility limit is noticed from Yb to Nd isomorph compounds.

These values are reported in table 5 as well as local CAS composition around the RE-cyclosilicate crystals. Contrary to the compositions established from the dissolution of RE_2O_3 powders (table 4), this CAS melt composition becomes richer in Ca and lower in Si and Al. This is in accordance with the dissolution of Ca-rich $Ca_3RE_2(Si_3O_9)_2$ cyclosilicate. However, the differences in CAS composition resulting from RE_2O_3/CAS and RE-cyclosilicate/CAS experiments (table 4 vs table 5) are relatively low due to the limited liquid field in CaO-Al_2O_3-SiO_2 system at 1200°C [24]. This implies that both systems may reasonably be

considered as comparable and that RE-cyclosilicate is stable in CAS whatever the RE-oxide mixed with (RE_2O_3 or RE-cyclosilicate).

4. Discussion

The discussion of the results is based on the $CaO\text{-}SiO_2\text{-}REO_{1.5}$ produced by Poerschke *et al.* at 1400°C (with RE = Gd and Y) [11,12]. Indeed, the nature of the precipitated phases observed here is the same for all the rare earths considered in this study, and none of them contains Al. However, the reader must keep in mind that the liquid domains of the phase diagrams might be modified as (i) the results discussed here were produced at 1200°C, and (ii) the initial molten silicate contains alumina Al_2O_3. Indeed, in the case of this study, the existence of a liquid domain enriched in SiO_2 is possible at 1200°C, due to the existence of a eutectic in the $CaO\text{-}SiO_2\text{-}Al_2O_3$ system.

The dissolution mechanism for all the rare earths is the same as that of Gd_2O_3 [13] and results in a very fast formation of RE-apatite at the interface with RE_2O_3. The apatite phase is locally in equilibrium with the oxide but not with the melt. This drives soon thereafter the RE-apatite dissolution into the unsaturated CAS to form the more stable cyclosilicate phase overtime. However, differences can be observed between the various RE_2O_3 on the solubility limits in CAS melt, as well as on the reaction kinetics and the RE-silicates crystal growth.

In nuclear aluminoborosilicate glasses [25, 26], in addition to the spontaneous precipitation of RE-apatites, they also noticed the more favorable formation when the ionic radius of the incorporated rare earth is close to that of Ca^{2+}. Indeed, apatite structure offers two types of sites for cationic species with high coordination numbers (i.e. more favorable for large cations): 6h sites and 4f sites with coordination numbers of 7 and 9 respectively. All 6h sites are occupied by 6 RE^{3+} cations whereas 4f sites are occupied by both RE^{3+} and Ca^{2+} cations. The two types of cations occupy 4f sites, and the larger the RE^{3+} cations are, the more favorable the formation of apatite phase is. The values reported in Table 6 clearly show that the difference of ionic radii between Ca^{2+} and RE^{3+} is maximum for Yb^{3+} and minimum for Nd^{3+}. This can explain, here, the favored precipitation of RE-apatite when ionic radii are increasing from Yb to Nd. Furthermore, assuming the same trend in stability as that of Ca-free apatites (with RE = La, Sm, Nd and Gd) [27], the formation enthalpy for $Ca_2RE_8(SiO_4)_2$ would effectively become lower (more favorable) when the ionic radius of rare earth increases (from Yb to Nd).

On the contrary, data concerning the formation enthalpies of RE-cyclosilicate $Ca_3RE_2Si_6O_{18}$ phases (which is isotype of $Ca_3Y_2Si_6O_{18}$ [23]) are not available. Due to its crystal structure, the precipitation of cyclosilicate might involve a complicated rearrangement of the silicate network to three-fold rings of Si_3O_9. This may explain the much faster crystallization of apatite over cyclosilicate. In the case of nuclear glasses [25], the formation of a phase with formula $Ca_{1-3x}RE_{2x}SiO_3$ (with x ~ 0.18) has been observed and may be similar to cyclosilicate. The precipitation of this phase seems to be favored for the rare earths with smaller ionic radii (from Y to Lu), which is consistent with the results observed here. In cyclosilicate phases, the cations can occupy 3 kinds of sites with coordination numbers of 6 (1 site), 7 (2 sites) and 8 (3 sites) [23]. The 3 types of sites are occupied by both Ca^{2+} and Y^{3+} cations: the smallest sites (CN = 6) are preferentially occupied by the small cations (i.e. Y^{3+}), and the largest sites (CN = 8) are preferentially occupied by the large cations (i.e. Ca^{2+}).

The late formation of cyclosilicate for the rare earths with larger ionic radius might be due (i) to the antagonist effects of the RE^{3+} cations size on the crystal structure and on the stability of both apatite and cyclosilicate phases, (ii) to kinetics aspects linked for instance to a modification of the glass network (number of three-fold rings of Si_3O_9) depending of the amount and the nature of RE^{3+} dissolved in the melt.

The reactivity of RE_2O_3 in silicate melts can also be discussed in considering the oxo-basicity theory [29], which is linked to the polarization of the M-O bond. Many equivalent criteria based on the RE effective charge (Z) and ionic radius (r) account for bond strength such as cation polarizability, RE ionic potential (Z/r) or RE^{3+} cation field strength (Z/r^2) [30]. The optical basicity concept can also be used to define metal oxides weakly bonded [31]. Cation field strength (Z/r^2) of the different RE^{3+} cations has thus been evaluated and reported in table 6. In a first approach, ionic radii corresponding to a coordination number equal to 6 have been chosen [32]. On figure 7, we have reported the solubility limits of RE in CAS, determined from RE_2O_3 and RE-cyclosilicate dissolution experiments (tables 4 and 5), as a function of RE^{3+} field strength. When starting from cyclosilicate powders, $Ca_3RE_2(Si_3O_9)_2$ is the unique and the stable phase overtime, the reported values (filled circles) are thus the solubility limit of this phase in CAS at 1200°C.

When starting from RE_2O_3, with RE = Nd, Sm or Gd, only RE-apatite is in contact with CAS for several hours. Consequently, the at. %(RE) values reported in figure 7 (filled

squares) are the solubility limits of the corresponding RE-apatites. Those values are higher than that for the stable cyclosilicate, which is characteristic of a RE oversaturation in the CAS. For Dy and Yb, the situation is different as several phases simultaneously precipitate: the measured RE contents can thus not be compared to those obtained with the other rare earths. Additional experiments have therefore been performed at higher temperatures (from 1250°C to 1400°C) to promote RE-apatite crystallization. Durations of 4 hours have been chosen, with addition of 20 wt. % RE_2O_3 in CAS. The aim was to measure the solubility limit of the high temperature phase and then to extrapolate it down to 1200°C assuming Arrhenius temperature dependence. Linear correlation between ln (at. %(RE)) and the reciprocal temperature has been found (Fig. 8). In the case of dysprosium, only apatite is detected at high temperature, and the value extrapolated at 1200°C (1.10 at. %(Dy)) is close to the measured one (1.17 at. %(Dy), table 4). This confirms that the measured value, despite the presence of precipitated cyclosilicate, is a dysprosium oversaturation in the melt, corresponding to metastable equilibrium between Dy-apatite and CAS melt.

The behavior of ytterbium is different as the stable phase observed at high temperature is not Yb-apatite but disilicate $Yb_2Si_2O_7$. The extrapolation of Yb content down to 1200°C leads to a value of 1.75 at. %(Yb) which is much higher than the measured one (0.99 at. %(Yb), table 4). Considering the high difference between these values, it can be assumed that the measured Yb content is not the solubility limit of Yb-disilicate. However, it cannot be really stated that it corresponds to the Yb-apatite solubility limit.

Thus, the two sets of data displayed on figure 7, are associated to the solubility limit in CAS melt at 1200°C of the different RE-apatites and RE-cyclosilicates. It can be first observed that the RE equilibrium concentration in the liquid with respect to RE-cyclosilicate is systematically lower than that of RE-apatite phase. This is in accordance with the greater stability of cyclosilicate in this system. In addition, the figure 7 clearly shows that the driving force for both apatite and cyclosilicate dissolution process significantly increases with its basicity.

Indeed, to dissolve in melts, RE_2O_3 reacts with silicate network according to an acid-base reaction, RE_2O_3 and CaO are basic oxides and SiO_2 is an acidic oxide. In the case of this CAS, which is peralkaline (CaO/Al_2O_3 >1), silica SiO_2 and alumina Al_2O_3 are network formers whereas RE_2O_3 and CaO are network modifiers. The latter, would convert Si-O

bridging oxygen (B.O) into non-bridging oxygen (NBO) to enter in the glass structure. Consequently, the dissolution of RE_2O_3 in acidic CAS will increase with its basicity. The link between acido-basicity and cation solubility has also been highlighted on the dissolution of chromium species in molten silicates [33]. On one hand, Cr^{VI} which has a small radius and a high electric charge (and thus a high Z/r^2) is very acidic and exhibits a higher solubility limit when it is dissolved in silicate melts of increasing basicity. On the other hand, basic Cr^{II} (low Z/r^2) sees its solubility limit increasing in melts with low basicity. In the same way, similar behavior is observed for cerium (Ce^{III} and Ce^{IV}) in borosilicate melts [34, 35].

5. Conclusion

The influence of rare earth on the reaction kinetics, solubility limits and phase equilibria of RE_2O_3 and $Ca_3RE_2(Si_3O_9)_2$ (RE = Nd, Sm, Gd, Dy, Yb) was studied at 1200°C in pseudo-ternary CAS melt using powders enclosed in glass-beads. This investigation follows previous work on Gd_2O_3 dissolution mechanisms in CAS, which is relevant to the development of CMAS resistant TBC.

For all RE_2O_3, indirect dissolution in CAS melt first occurred and was controlled by interface reaction resulting in RE-apatite formation. The kinetics of RE-apatite crystal growth and their solubility limit was found to be enhanced for Nd, Sm and Gd compared to Yb and Dy. During early-stage of interaction, Yb-disilicate was competitively crystallized around Yb_2O_3 powders. For longer durations, RE-cyclosilicate phase, which precipitates at the expanse of metastable RE-apatite, was observed to be in equilibrium with CAS melt. Delay in RE-cyclosilicate phase nucleation increases from few minutes for Yb and Dy, to few hours for Gd and to hundred hours for Sm (and probably more for Nd). This delayed nucleation might be purely kinetic and/or linked to the respective stabilities of RE-apatites and RE-cyclosilicates.

The dissolution of synthetic RE-cyclosilicate in CAS melt was then investigated, exhibiting direct dissolution. The solubility limit and the time to reach equilibrium conditions were noticed to increase from Yb to Nd. RE-cyclosilicate solubility limits were also found to be lower than that of RE-apatite and disilicate phases. Relative stabilities of RE-apatite and RE-cyclosilicate were discussed in the light of crystal chemistry as well as thermodynamic considerations such as free energy of formation. The network modifier role of RE cations and

the cation field strength (Z/r^2) - which accounts for RE-O bond strength in crystals - were also used to describe RE-silicates (RE-apatite and RE-cyclosilicate) acid-base dissolution in CAS melt. Indeed, the RE solubility of the apatites or cyclosilicates coexisting with CAS melt was found to be inversely related to the magnitude of the different RE cation field strengths.

The results obtained on the behavior of rare-earth oxides in CAS melt may help in a comparative study of rare-earth zirconates interaction with CMAS. Indeed, it has been shown that RE cations with large radius will provide the larger volume of apatite during early stage of the reaction with CAS, which would be more effective to limit CMAS infiltration. However, as the RE-apatite solubility limit would be high, increasing from Gd to Nd, (considering also that large RE cations rather partition into the apatite than into the fluorite phase [14]), the amount of RE_2O_3 required to initiate RE-apatite precipitation would be higher, resulting in a higher TBC coating recession. The appearance of secondary phases with lowers RE solubility in melt, such as RE-cyclosilicates, may however be beneficial as they act as diffusion barriers between the sealing layer and the CMAS, thus limiting apatite redissolution.

Acknowledgements

The authors gratefully acknowledge O. Rouer (Service Commun de Microscopies Electroniques et Microanalyses X of the University of Nancy) and C. Sanchez (Onera, Université Paris Saclay) for performing electron-probe microanalysis and XRD respectively. This work was supported by the French Defense Research Organization (DGA).

References

[1] M.P. Borom, C.A. Johnson and L.A. Peluso, Role of environmental deposits and operating surface temperature in spallation of air plasma sprayed thermal barrier coatings, Surf. Coat. Technol., 86-87 (1996) 116-126.

[2] S. Krämer, J.Y. Yang, C.A. Johnson and C.G. Levi, J. Am. Ceram. Soc., 89 [10] (2006) 3167–3175.

[3] C. Mercer, S. Faulhaber, A.G. Evans and R. Darolia, A delamination mechanism for thermal barrier coatings subject to calcium–magnesium–alumino-silicate (CMAS) infiltration, Acta. Mater., 53 [4] (2005) 1029-1039.

[4] C.G. Levi, J.W. Hutchinson, M.H. Vidal-Sétif and C.A. Johnson, Environmental degradation of thermal-barrier coatings by molten deposits, MRS bulletin, vol 37 n°10 (2012) 932-941.

[5] M.H. Vidal-Setif, N Chellah, C Rio, C Sanchez, O. Lavigne, Calcium–magnesium–alumino–silicate (CMAS) degradation of EB-PVD thermal barrier coatings: characterization of CMAS damage on ex-service high pressure blade TBCs, Surf. Coat. Technol., 208 (2012) 39–45.

[6] J.L. Smialek, The chemistry of Saudi Arabian sand: a deposition problem on helicopter turbine airfoils, NASA TM-105234, NASA Lewis Research Center (1991).

[7] W. Braue, P. Mechnich, Recession of an EB-PVD YSZ coated turbine blade by $CaSO_4$ and Fe, Ti-rich CMAS-type deposits, J. Am. Ceram. Soc., 94 (2011) 4483-4489.

[8] S. Krämer, J. Yang, C.G. Levi, Infiltration-inhibiting reaction of gadolinium zirconate thermal barrier coatings with CMAS melts, J. Am. Ceram. Soc., 91 (2008) 576-583.

[9] J. Felsche, Rare earth silicates with the apatite structure, J. Solid. State Chem., 5 (1972) 266-275.

[10] C. Wang, M. Zinkevich, F. Aldinger, Phase diagrams and thermodynamics of rare-earth-doped zirconia ceramics, Pure Appl. Chem., 79 (2007) 1731-1753

[11] D.L. Poerschke, T. L. Barth, O. Fabrichnaya, C. G. Levi, Phase equilibria and crystal chemistry in the calcia–silica–yttria system, J. Eur. Ceram. Soc., 36 (2016) 1743-1754.

[12] D. L. Poerschke, C. G. Levi, Phase equilibria in the calcia-gadolinia-silica system, J. Alloys Compd., 695 (2017) 1397-1404

[13] F. Perrudin, C. Rio, M.H. Vidal-Sétif, C. Petitjean, P.J. Panteix, M. Vilasi, Gadolinium oxide solubility in molten silicate: dissolution mechanism and stability of $Ca_2Gd_8(SiO_4)_6O_2$ and $Ca_3Gd_2(Si_3O_9)_2$ silicate phases, J. Eur. Ceram. Soc., 37 (2017) 2657-2665.

[14] D. L. Poerschke, Talia L. Barth, C. G. Levi, Equilibrium relationships between thermal barrier oxides and silicate melts, Acta. Mater., 120 (2016) 302-314.

[15] D. L. Poerschke, C. G. Levi, Effects of cation substitution and temperature on the interaction between thermal barrier oxides and molten CMAS, J. Eur. Ceram. Soc., 35 (2015) 681-691.

[16] U. Schulz, W. Braue, Degradation of $La_2Zr_2O_7$ and other novel EB-PVD thermal barrier coatings by CMAS ($CaO\text{-}MgO\text{-}Al_2O_3\text{-}SiO_2$) and volcanic ash deposits, Surf. Coat. Technol., 235 (2013) 165–173.

[17] R. W. Jackson, E. M. Zaleski, B. T. Hazel, M. R. Begley, C. G. Levi, Response of molten silicate infiltrated Gd2Zr2O7 thermal barrier coatings to temperature gradients, Acta Mater., 132 (2017) 538-549.

[18] J.M. Drexler, A. L. Ortiz, N. P. Padture, Composition effects of thermal barrier coating ceramics on their interaction with molten Ca–Mg–Al–silicate (CMAS) glass, Acta. Mater., 60 (2012) 5437–5447.

[19] M.H. Vidal-Sétif, C. Rio, D. Boivin and O. Lavigne, Microstructural characterization of the interaction between 8YPSZ (EB-PVD) thermal barrier coatings and a synthetic CAS, Surf. Coat. Technol., 239 [41] (2014).

[20] P.J. Panteix, I. Julien, D. Bernache-Assollant, P. Abelard, Synthesis and characterization of oxide ions conductors with the apatite structure for intermediate temperature SOFC, J. Mater. Chem. Phys., 95 (2006) 313-320.

[21] O. Delattre, E. Regnier, S. Schuller, M. Allix, G. Matzen, Image analysis study of crystallization in two glass compositions of nuclear interest, J. Non-Cryst. Solids, 379 (2013) 112-122.

[22] U. Kolitsch, H. J. Seifert, F.Aldinger, Phase relationships in the systems RE_2O_3-Al_2O_3-SiO_2, J. Phase Equilib., 19 (5) (1998) 426-433.

[23] H. Yamane, T. Nagasawa, M. Shimada and T. Endo, $Ca_3Y_2(Si_3O_9)_2$, Acta Cryst., C53 (1997) 1533-1536.

[24] H. Mao, M. Hillert, M. Selleby, B. Sundman, Thermodynamic assessment of the CaO-Al_2O_3-SiO_2 system, J. Am. Ceram. Soc., 89 (2006) 298-308.

[25] A. Quintas, D. Caurant, O. Majérus, J.-L Dussossoy, T. Charpentier, Effect of changing the rare earth cation type on the structure and crystallisation behaviour of an aluminoborosilicate glass, Physics and Chemistry of Glasses - Glass Technol.: Eur. J. Glass Sci. Technol., Part B, 49 (2008) 192-197

[26] A. Kidari, J.L. Dussossoy, E. Brackx, D. Caurant, M. Magnin, I. Bardez-Giboire, Lanthanum and Neodymium Solubility in Simplified SiO_2–B_2O_3–Na_2O–Al_2O_3–CaO High Level Waste Glass, J. Am. Ceram. Soc., (2012) 1–8

[27] A. Risbud, K. Helean, M. Wilding, P. Lu, A. Navrotsky, Enthalpies of formation of lanthanide oxyapatite phases, J of Mater. Res., 16 [10] (2001) 2780-2783.

[28] A. Quintas, Etude de la structure et du comportement en cristallisation d'un verre nucléaire d'aluminoborosilicate de terre rare, PhD dissertation (2007), Université Pierre et Marie Curie. Retrieved from https://tel.archives-ouvertes.fr/pastel-00003519.

[29] H. Flood, T. Forland, The acidic and basic properties of oxides, Acta. Chem. Scand., 1 (1947) 592-604.

[30] A. Dietzel, Die Kationenfeldstärken und ihre Beziehungen zu Entglasungsvorgängen, zur Verbindungsbildung und zu den Schmelzpunkten von Silicaten, Z. Elektrochem. Angew., 48 (1942) 9-23.

[31] J. A. Duffy, M. D. Ingram, An interpretation of glass chemistry in terms of the optical basicity concept, J. of Non-Cryst. Solids, 21 (1976) 373-410.

[32] R. D. Shannon, Revised Effective Ionic Radii and Systematic Studies of Interatomic Distances in Halides and Chalcogenides, Acta Cryst., A32, (1976) 751-767.

[33] H. Khedim, S. Abdelouhab, R. Podor, C. Rapin, M. Vilasi, P-J. Panteix, M. Toplis, F. Faure, Kinetic and equilibrium factors affecting saturation of chromium oxide in soda-silicate melts, J. Non-Cryst. Solids, 357 (2011) 31-42.

[34] C. Lopez, X. Deschanels, J. M. Bart, J.M. Boubals, C. Den Auwer, E. Simoni, Solubility of actinide surrogates in nuclear glasses, J. Nucl. Mater., 312 (2003) 76-80

[35] J.N. Cachia, X. Deschanels, C. Den Auwer, O. Pinet, J. Phalippou, C. Hennig, A; Scheinost, Enhancing cerium and plutonium solubility by reduction in borosilicate glass, J. Nucl. Mater., 352 (2006) 182-189.

Figures

Figure 1. SEM micrographs of different RE_2O_3/CAS beads section annealed at 1200°C for 5 min. RE_2O_3 = Nd_2O_3 (a), Sm_2O_3 (b), Gd_2O_3 (c) and Dy_2O_3 (d).

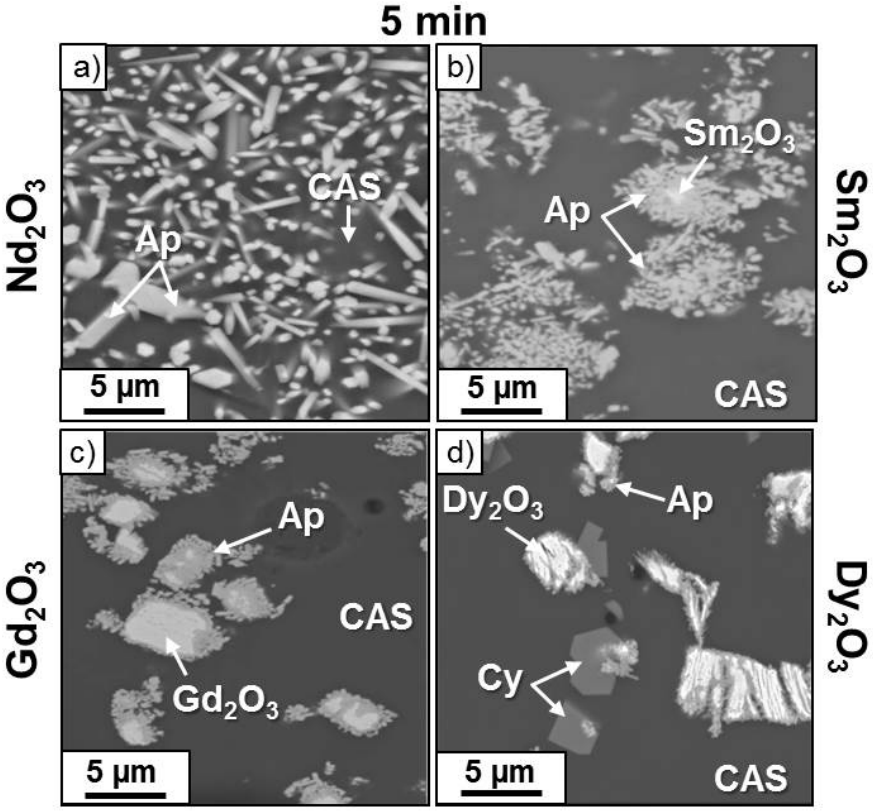

Figure 2. Low (a) and high (b) magnification SEM micrograph of a Yb_2O_3/CAS bead section annealed at 1200°C for 5 min. And corresponding Yb (Lα) (c) and Ca (Kα) (d) EDS elemental maps. The insert in figure 2a shows Yb_2O_3 surrounded by Yb-apatite crystals.

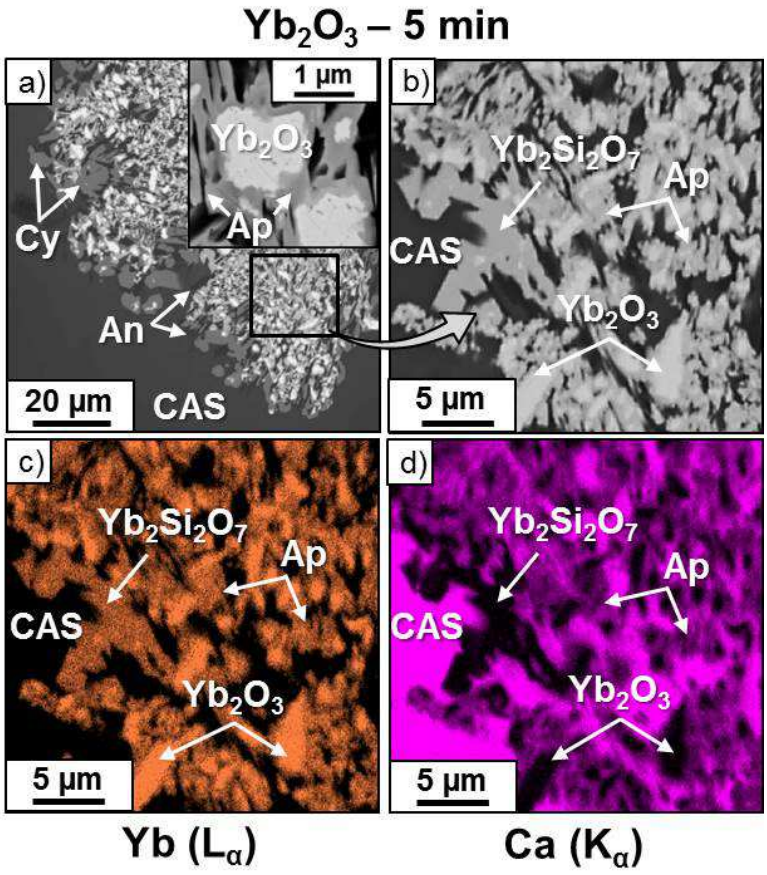

Figure 3. SEM micrographs of different RE_2O_3/CAS beads section annealed at 1200°C for 72 h: Gd_2O_3 (a), Dy_2O_3 (b), Nd_2O_3 (c) and Sm_2O_3 (d). And annealed at 1200°C for 160 h: Nd_2O_3 (e) and Sm_2O_3 (f).

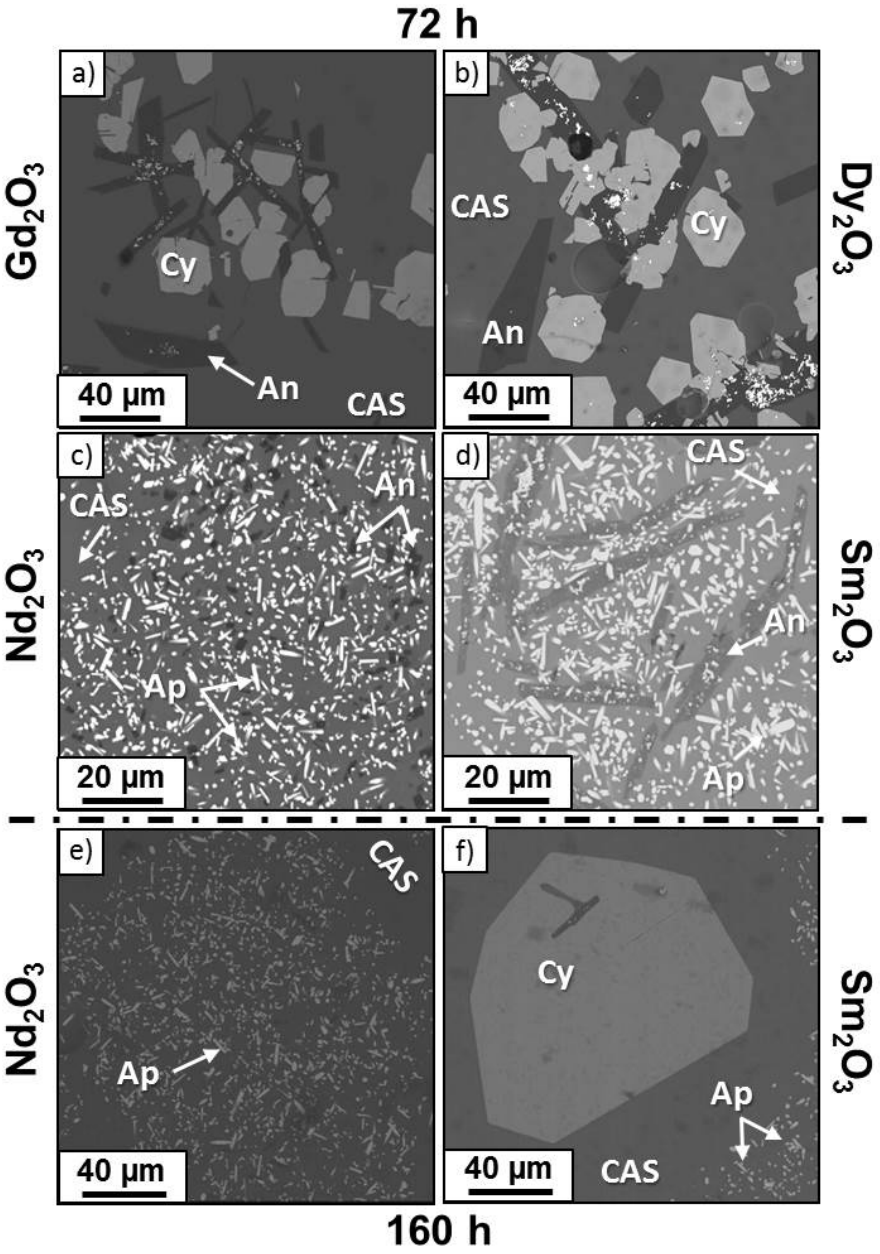

Figure 4. Rietveld refinement on XRD pattern of a 30/70 %wt. Gd_2O_3/CAS powder mixture annealed at 1200°C for 1 h (a). And RE-silicates (RE-apatite, RE-cyclosilicate and $RE_2Si_2O_7$) quantitative phase analysis of the different 30/70 %wt. RE_2O_3/CAS powder mixture (RE_2O_3 = Nd_2O_3, Sm_2O_3, Gd_2O_3, Dy_2O_3 and Yb_2O_3) annealed 1 h at 1200°C (b).

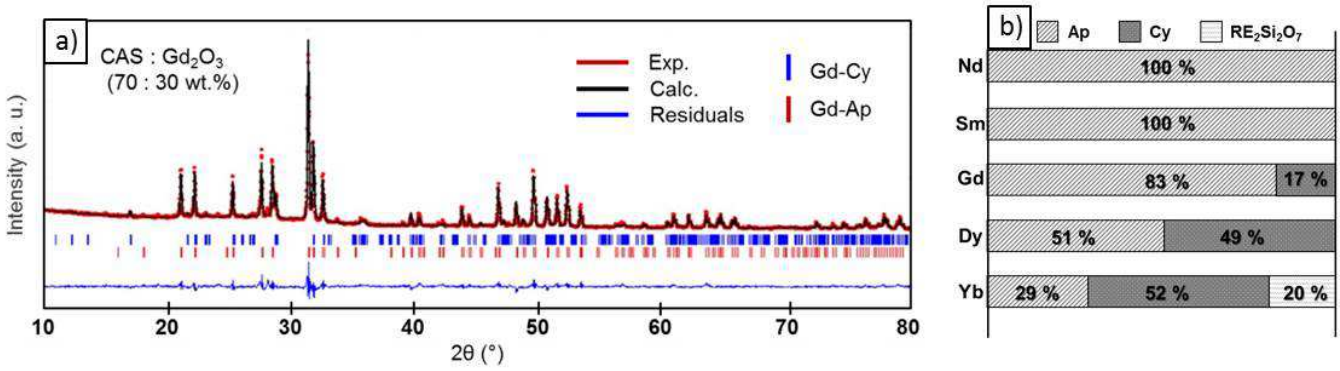

Figure 5. Evolution of the RE dissolved content in CAS melt at 1200°C as a function of the square root of time for Gd_2O_3, Sm_2O_3 and Nd_2O_3 (a) and Yb_2O_3, Dy_2O_3 (b) CAS beads mixture.

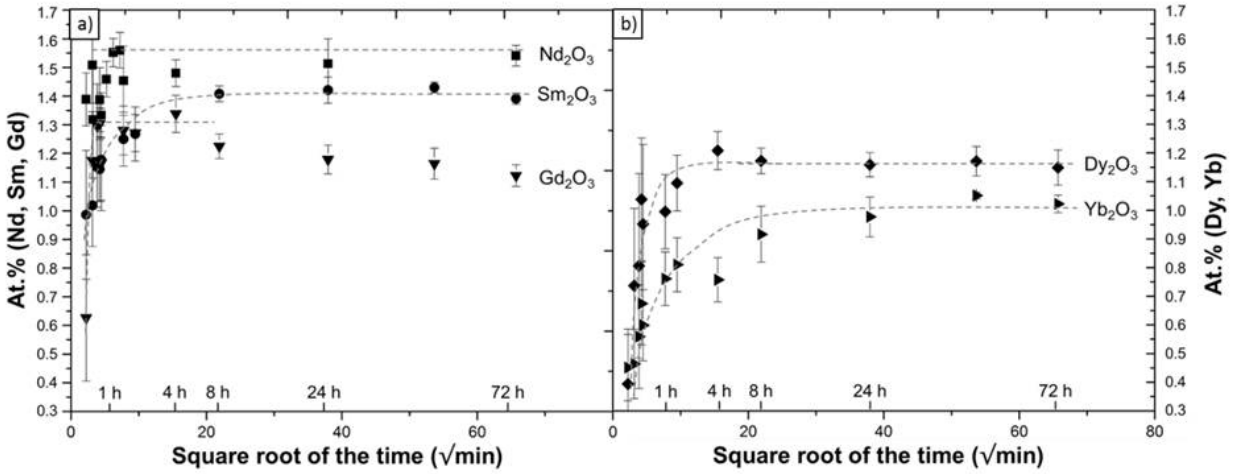

Figure 6. Evolution of the RE dissolved content in CAS melt at 1200°C as a function of the square root of time for Gd, Sm and Nd-cyclosilicate (a) and Yb, Dy-cyclosilicate (b) CAS beads mixture.

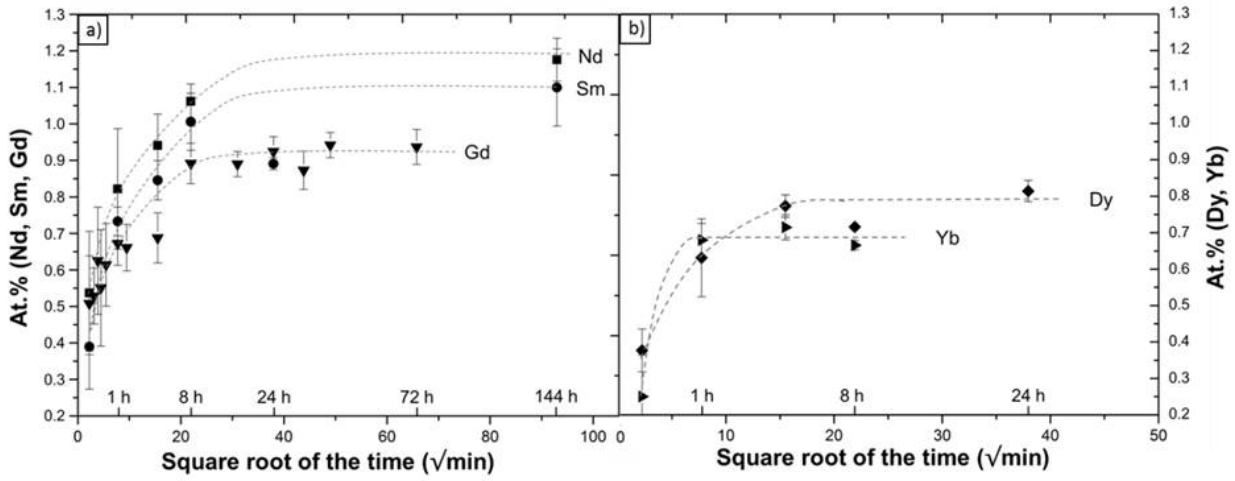

Figure 7. RE solubility limits in CAS melt at 1200°C of the different RE-silicate phases (RE-apatite and RE-cyclosilicate) determined from RE_2O_3 and RE-cyclosilicate dissolution experiments, as a function of cation field strength. Optical basicity (OB) values of RE_2O_3 have also been reported on the X-axis.

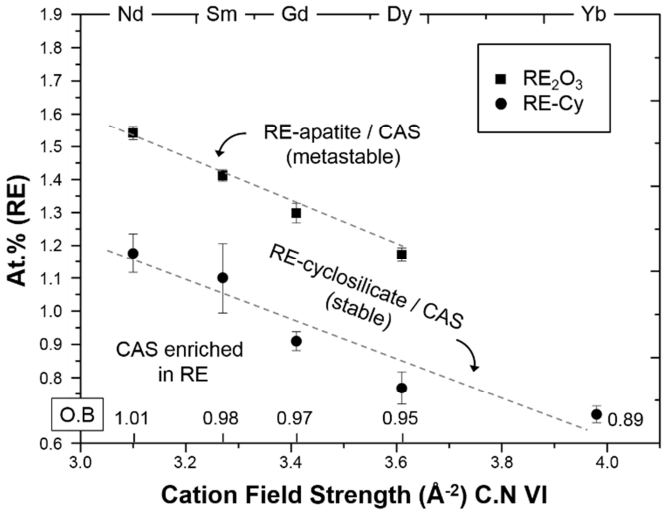

Figure 8. Arrhenius plot of the RE content dissolved in CAS (ln(At.%RE)) as a function of the reciprocal temperature (1/T) for Yb_2O_3 and Dy_2O_3/CAS beads mixture annealed at 1400, 1350, 1300 and 1250°C for 4 h and then extrapolated down to 1200°C.

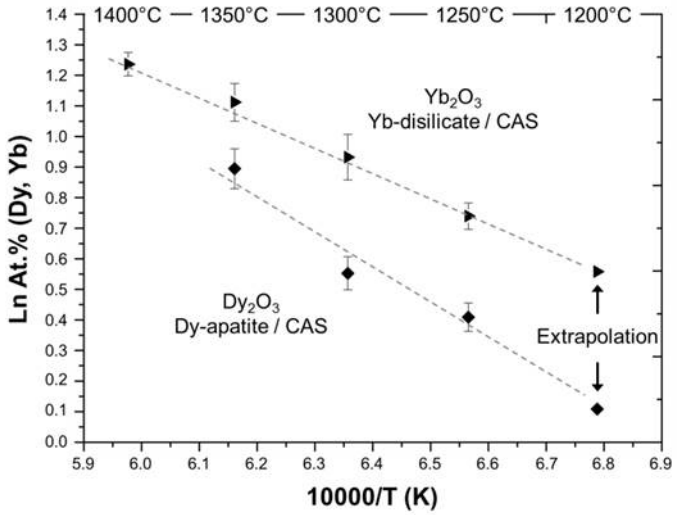

Tables

Table 1. Purity, median granulometry and crystalline structure of the different RE_2O_3 commercial powders

	Nd_2O_3	Sm_2O_3	Gd_2O_3	Dy_2O_3	Yb_2O_3
Supplier	Treibacher	Treibacher	Cerac	Ampere	Treibacher
Purity (%)	99.87	99.99	99.90	>99.90	99.99
d_{50} (µm)	2.20	3.60	/	3.00	1.03
Crystal. structure	Hexagonal	Mono + cubic	Cubic	Cubic	Cubic

Table 2. Overall composition in mol. % of single cation oxide for the CAS+RE-oxide mixtures (RE = Nd & Yb) and correlation with the wt. % of solute added to CAS

Solute	Wt. %	Composition in mol. % of singe cation oxide			
		CaO	$AlO_{1.5}$	SiO_2	$REO_{1.5}$
/	/	24.1	16.9	58.9	/
Yb_2O_3	10	23.4	16.4	57.1	3.1
Nd_2O_3	15	22.8	16.0	55.6	5.7
Yb-Cy	15	24.4	15.4	58.5	1.7
Nd-Cy	60	25.1	11.8	57.6	5.5

Table 3. Timeline of the different RE_2O_3/CAS reactive sequence after annealing beads mixtures at 1200°C.

Silicate melt	Solute	RE_2O_3 entirely converted	RE-apatite formation	RE-cyclosilicate formation
CAS	Nd_2O_3	≤ 5 min	≤ 5 min	> 160 h
CAS	Sm_2O_3	15 min	≤ 5 min	160 h
CAS	Gd_2O_3	90 min	≤ 5 min	90 min
CAS	Dy_2O_3	4 h	≤ 5 min	≤ 5 min
CAS	Yb_2O_3	24 h	≤ 5 min	≤ 5 min

Table 4. EPMA elemental composition of CAS glasses (averaged from the 4 latest points at the plateau) in contact with RE-apatite or RE-cyclosilicate obtained from RE_2O_3 indirect dissolution reaction.

Silicate melt	Solute	Phase in contact with CAS	CAS comp. at the plateau (at. % and mol % of single cation oxide)				
			Ca	Al	Si	RE	O
CAS theoretical composition			9.0	6.3	22.1	0.00	62.6
			24.1	16.9	58.9	0.00	/
CAS	Nd_2O_3	Ap	8.75 (0.07)	6.24 (0.03)	21.00 (0.04)	**1.54** (0.02)	62.47 (0.07)
			23.32 (0.17)	16.63 (0.07)	55.94 (0.14)	**4.11** (0.06)	/
CAS	Sm_2O_3	Ap	8.70 (0.05)	6.25 (0.05)	21.14 (0.05)	**1.41** (0.02)	62.49 (0.08)
			23.20 (0.12)	16.66 (0.12)	56.37 (0.15)	**3.77** (0.05)	/
CAS	Gd_2O_3	Ap	8.80 (0.03)	6.50 (0.02)	21.00 (0.02)	**1.30** (0.03)	62.40 (0.04)
			23.31 (0.06)	17.18 (0.05)	56.05 (0.08)	**3.46** (0.08)	/
CAS	Dy_2O_3	Cy	8.60 (0.13)	6.47 (0.07)	21.21 (0.15)	**1.17** (0.03)	62.54 (0.13)
			22.86 (0.25)	17.21 (0.09)	56.82 (0.20)	**3.11** (0.04)	/
CAS	Yb_2O_3	Cy	8.94 (0.05)	6.25 (0.02)	21.33 (0.03)	**0.99** (0.07)	62.48 (0.11)
			23.82 (0.12)	16.66 (0.04)	56.85 (0.10)	**2.66** (0.18)	/

Table 5. EPMA elemental composition of CAS glasses (averaged from the 3 latest points at the plateau for Yb, Dy and Gd-cyclosilicate/CAS beads) obtained from direct dissolution of synthetic RE-cyclosilicate.

Silicate melt	Solute	Phase in contact with CAS	CAS comp. at the plateau (at. % and mol % of single cation oxide)				
			Ca	Al	Si	RE	O
CAS theoretical composition			9.0	6.3	22.1	0.00	62.6
			24.1	16.9	58.9	0.00	/
CAS	Nd-Cy	Cy	9.31 (0.05)	5.26 (0.06)	21.52 (0.06)	**1.18** (0.06)	62.73 (0.08)
			24.98 (0.14)	14.11 (0.17)	57.75 (0.20)	**3.16 (0.16)**	/
CAS	Sm-Cy	Cy	9.27 (0.07)	5.79 (0.19)	21.18 (0.27)	**1.10** (0.11)	62.66 (0.25)
			24.83 (0.14)	15.51 (0.49)	56.72 (0.83)	**2.95 (0.28)**	/
CAS	Gd-Cy	Cy	9.11 (0.03)	5.84 (0.04)	21.65 (0.03)	**0.91** (0.03)	62.49 (0.05)
			24.30 (0.07)	15.53 (0.09)	57.74 (0.09)	**2.43** (0.08)	/
CAS	Dy-Cy	Cy	9.38 (0.05)	5.64 (0.11)	21.68 (0.16)	**0.77** (0.05)	62.53 (0.11)
			25.04 (0.17)	15.05 (0.31)	57.86 (0.37)	**2.05** (0.13)	/
CAS	Yb-Cy	Cy	9.42 (0.06)	5.59 (0.07)	21.82 (0.04)	**0.69** (0.03)	62.48 (0.07)
			25.10 (0.13)	14.90 (0.19)	58.16 (0.09)	**1.83** (0.07)	/

Table 6 . Optical basicity of the different RE_2O_3, RE ionic radius in coordination number VI and relative difference with Ca ionic radius $\Delta r/r_0$ (%), RE cation field strength Z/r^2 (Z : effective charge and r : ionic radius).

	Optical Basicity (OB)	Ionic (+III) radius (VI, Å)	$\%\Delta r/r_0$ (Ca-RE/Ca)	Z/r^2 (VI)
Nd_2O_3	1.01	0.983	1.7	3.10
Sm_2O_3	0.98	0.958	4.2	3.27
Gd_2O_3	0.97	0.938	6.2	3.41
Dy_2O_3	0.95	0.912	8.8	3.61
Yb_2O_3	0.89	0.868	13.2	3.98
CaO	1.00	1.000	/	2.00